Electrochimica Acta 476 (2024) 143723

Contents lists available at ScienceDirect

Electrochimica Acta

journal homepage: www.journals.elsevier.com/electrochimica-acta

Unveiling the impact of laser power variations on microstructure, corrosion, and stress-assisted surface crack initiation in laser powder bed fusion-processed Ni-Fe-Cr alloy 718

Arshad Yazdanpanah [a,*], Reynier I. Revilla [b,*], Mattia Franceschi [a], Alberto Fabrizi [c], Saeed Khademzadeh [a,d], Mona Khodabakhshi [e], Iris De Graeve [b], Manuele Dabalà [a]

[a] Department of Industrial Engineering, University of Padova, Via Marzolo 9, 35131 Padova, Italy
[b] Department of Materials and Chemistry, Research Group Electrochemical and Surface Engineering, Vrije Universiteit Brussel (VUB), Pleinlaan 2, 1050 Brussels, Belgium
[c] Department of Engineering and Management, University of Padova, Vicenza, 36100, Italy
[d] Department of Manufacturing Processes, RISE research institutes of Sweden, Argongatan 30, 431 53 Mölndal, Sweden
[e] Department of Information Engineering, University of Padova, Via Gradenigo, 6/b - 35131 Padova, Italy

ARTICLE INFO

Keywords:
Additive manufacturing
Laser powder bed fusion
Stress corrosion cracking
Localized corrosion
Electrochemical polarization
Microcapillary electrochemical technique

ABSTRACT

Corrosion and stress-corrosion related failures often compromise the integrity of critical metallic components during their service, raising significant concerns. It is crucial to comprehend the crack initiation mechanism and the impact of alloy microstructure on this crack initiation process. It is known that the introduction of unique microstructures through metal additive manufacturing brings new challenges. This study aims to investigate, for the first time, the effects of microstructural alterations resulting from fluctuations in laser power during laser powder bed fusion on the surface cracking initiation mechanism and electrochemical behaviour of Ni-Fe-Cr alloy 718, which is widely used in applications that require exceptional strength and corrosion resistance. To carry out this investigation, microcapillary electrochemical methods were combined with high-resolution techniques (TEM, SEM, AFM). The findings emphasize the existence of an optimal range of process parameters that effectively mitigate corrosion and crack initiation susceptibility. This work demonstrated that slight deviations in laser power from this optimal value result in diverse alterations at the micro and submicron scales. These alterations include increased subgrain width, porosity, dislocation density, density of nanovoids, and distribution of carbides. Importantly, these changes, particularly in dislocation and nanovoid densities caused by minor variations in process parameters, significantly affect the material's susceptibility to corrosion initiation and stress-assisted surface cracking.

1. Introduction

Ageing of currently in-service critical components in oil, gas, and nuclear industries is one of the major concerns, while, the regular substitution of degraded components is a common practice in sensitive industries to avoid catastrophic incidences [1]. In the past decade, metal additive manufacturing (MAM) has emerged as a promising technique capable of replacing conventional methods for the fabrication of intricate geometries with near-full density [2]. Laser powder bed fusion (L-PBF) is among the most precise MAM techniques which are widely employed for the fabrication of parts wherein, high-quality assurance is required [2]. Thus, L-PBF could be the primary candidate technique for the fabrication of substitutive critical nickel-based components, in which, their production with conventional manufacturing methods requires extensive time, energy, and equipment. The inherent microstructure of L-PBF processed materials generally consists of submicron columnar/cellular structure with highly decorated subgrain boundaries, which are generally enriched in certain alloying elements, depending on the alloy type [3–8]. Alloy 718 is a nickel-iron-chromium-based superalloy that has been used in highly demanding corrosive environments in gas and oil (e.g., downhole components, drilling tools, and seal assemblies), marine, and nuclear industries (e.g., control rods fasteners and valves), where exceptional strength and corrosion resistance are required. Over the last decade, significant research efforts have been

* Corresponding authors.
E-mail addresses: arshad.yazdanpanah@phd.unipd.it (A. Yazdanpanah), rrevilla@vub.be (R.I. Revilla).

https://doi.org/10.1016/j.electacta.2023.143723
Received 16 September 2023; Received in revised form 26 November 2023; Accepted 27 December 2023
Available online 27 December 2023

devoted to exploring the optimization of process parameters and its association with the mechanical, creep, and fatigue properties of Laser Powder Bed Fusion (L-PBF) processed alloy 718 [4,9]. However, to the best of our knowledge, the impact of short-range variation within the optimal process parameters on microstructural characteristics and corrosion performance has not been conclusively determined.

Among the various types of environmentally assisted degradations, stress corrosion cracking (SCC) has been widely considered the most critical type, as a consequence of the prolonged incubation-initiation period and its catastrophic nature [10]. The occurrence of SCC is a result of the complex interplay between environmental factors and the presence of tensile stresses. Notably, SCC can readily occur even under tightly regulated conditions of water chemistry, as observed in environments such as boiling water reactors (BWR) and pressurized water reactors (PWR) where nickel-based alloys are employed [11,12]. Thus, the incidence of SCC is inevitable, and the main question is how severe the crack initiation and propagation rates are before reaching a critical rate. Despite extensive research on the corrosion behaviour of MAM-processed materials in various environments, SCC characteristics have received very limited attention and the correlation of process parameters with SCC occurrence is not clear. The few existing publications are mostly focused on austenitic stainless steels considering the propagation stage of cracks and the comparison with conventional counterparts. For instance, Lou et al. [13,14], reported the formation of cracks in both low-angle boundaries corresponding to subgrains boundaries and high-angle boundaries corresponding to larger elongated grains after heat treatment, postulating selective dissolution of oxide inclusions along the subgrain boundaries to be the cause of the formation of the cracks at low-angle boundaries. Song et al. [15], reported higher susceptibility of as-built L-PBF 316 L to irradiation-induced SCC growth compared to conventional counterparts, while, McMurtrey et al. [16] reported the contrary case. Karasz et al. [17], studied SCC susceptibility in boiling magnesium chloride solution, highlighting the correlation of SCC to the residual stress state of the L-PBF 316 L. In a recent study by Cruz et al. [18], utilizing slow strain rate SCC study of L-PBF 316 L, they indicated higher SCC resistance compared to the wrought counterpart, relating this behaviour with the higher localized corrosion resistance of the L-PBF case compared to the wrought material due to the absence of MnS inclusions. For the case of MAM-processed Ni-based alloys, the number of research articles is even more limited, and the SCC behaviour is still not clear. For instance, Cabrini et al. [19] investigated the SCC propagation of alloy 625, indicating high resistance of L-PBF specimens to chloride induced SCC in boiling magnesium chloride solution as a result of smaller size of secondary phases compared to conventional counterpart, leading to less hydrogen uptake and embrittlement during tensile straining. However, boiling magnesium chloride solution could give contradictory results for Ni-based alloys as extensively investigated over the past decades due to the extreme alteration of the environment compared to actual conditions [12,20]. In fact, Coriou et al. [12] revealed that SCC could readily occur in even deoxygenated pure water under the presence of tensile stresses (as the most critical factor) for alloy 600, which was considered immune to SCC formation under the test condition with boiling magnesium chloride environment. Furthermore, Yong et al. [21], conducted a study to investigate the impact of heat treatment on the stress corrosion cracking (SCC) behaviour of L-PBF 800H. Their findings revealed varying crack growth behaviour, which exhibited a high sensitivity to local microstructural inhomogeneities.

Although the incubation-initiation stage of crack occurrence is the most important and critical stage for life assessment in industrial applications, and even though having delayed crack initiation could directly increase the lifetime of the components, few researchers have addressed this stage of cracking for conventionally manufactured components [22–31], and additively manufactured specimens (works by the authors) [32–34]. A major difficulty with this type of study is related to the detection of such events, as a consequence of extremely small and highly localized sites. In the authors' previous investigation [35], for the first time, an attempt was made to elucidate stress-assisted cracking initiation susceptibility by implementing the microcapillary electrochemical method. The crack initiation mechanism in L-PBF 718 was elucidated through the synergistic interplay of selective dissolution of the subgrain matrix, the creation of a coupled environment at the subgrain level, and the high density of dislocations. These factors were identified as the key contributors to crack initiation occurring adjacent to subgrain boundaries [35]. This work revealed significantly lower susceptibility to crack initiation for L-PBF-fabricated parts compared to conventional alloy, by virtue of both substantially smaller cracks and less severity of cracking. A question that remains unanswered is to what extent L-PBF process parameters could affect the corrosion and crack initiation behaviour. To address this issue, a better understanding of the correlation between microstructural characteristics of L-PBF fabricated components (including their relationship with process parameters) and crack initiation susceptibility is of paramount importance.

In this pioneering academic investigation, the aim is to assess, for the first time, the influence of short-range variations in process parameters of the L-PBF process on the microstructural characteristics and susceptibility to corrosion and stress-assisted surface cracking of alloy 718. To achieve this objective, the study employs the microcapillary electrochemical technique. Electrochemical polarization experiments, in conjunction with accelerated tests, are conducted in chloride-containing aqueous solutions. These solutions are chosen due to their prevalence as the most common contamination in gas, oil, and nuclear industries located in coastal regions. The electrochemical tests are accompanied by a comprehensive analysis of the microstructure, providing a systematic characterization. The crack initiation susceptibility of L-PBF 718 specimens, fabricated with different energy input densities, is carefully assessed, and the mechanisms responsible for the observed variations are proposed.

2. Experimental methods

2.1. L-PBF processing and specimen preparation

Gas atomized powder of alloy 718 (UNS-N07718, identified by ASTM F3055–14a) with spherical particles in the range of 10–53 μm in diameter, and nominal chemical composition (provided by the manufacturer) as summarized in Table 1, was employed to fabricate cuboids with a dimension of 10 × 30 × 30 mm. SISMA 100 (SISMA Italy) laser metal fusion machine equipped with a 200 W fibre laser was utilized, by setting the laser diameter spot at 40 μm under an argon-controlled atmosphere (oxygen level below 200 ppm). A bidirectional alternating chessboard scan strategy (as shown in Fig. 1a) was employed by maintaining the layer thickness at 20 μm, hatch spacing at 70 μm, scan speed at 750 mm/s, chess island size of 4 × 4 mm, and three different values of laser power of 105, 115, and 125 W. The process parameters used in the current investigation were chosen based on the authors' previous investigation (in the same range) [35], with the intention of fabricating nearly fully dense specimens.

Cuboid samples were sliced perpendicular to the build direction, utilizing electro-discharge machining (EDM) to prepare the final specimens with a dimension of 10 × 30 × 0.8 mm. The first and last 1 mm thickness along the build direction were excluded in order to avoid possible microstructural variations caused by boundary effects. The specimens were ground and polished up to 0.1 μm alumina suspension to obtain a mirror finishing. Samples were subjected to ultrasonic washing for 15 min using a 10 % ethanol solution and rinsed with pure ethanol. To allow for the formation of a native oxide layer on the surface and to facilitate the redistribution of any residual stress alterations that may have occurred during the sample preparation, the samples were left undisturbed for a period of 72 h. A schematic view of the sample preparation is shown in Fig. 1b.

Table 1
Chemical composition of alloy 718 powder.

El	Ni	Cr	Fe	Nb	Mo	Ti	Al	Co	Si	Mn	Cu	C	P	N	B
wt.%	53.70	17.93	18.17	5.20	2.96	0.95	0.48	0.33	0.08	0.08	0.05	0.025	0.009	0.004	0.0025

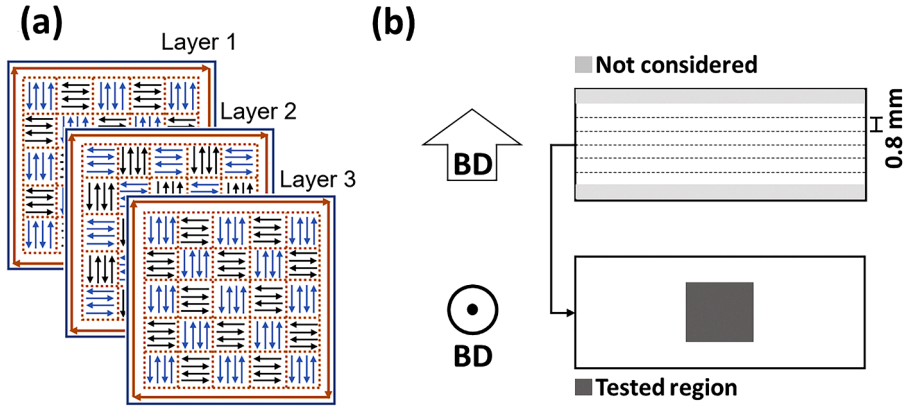

Fig. 1. (a) Alternating chess board strategy utilized for the fabrication of the specimens, and (b) sectioning of the fabricated specimens perpendicular to build direction (BD) and the desired zone for further investigations.

2.2. X-ray diffraction residual stress and hardness measurements

The residual stresses of the specimens were measured utilizing X-ray diffraction method. Residual stress measurements of the as-built specimens were conducted using a Spider TM X GNR portable diffractometer operating at 30 kV and 90 μA, with a Cu K-α radiation source. The sin2 (ψ) method was implemented by choosing the {311} plane (austenitic peak) as the diffraction peak and the variation of 2θ angle between 0° and 43° with a total of 9 angles. Residual stress measurements using X-ray diffraction were carried out at the centre of the specimens. The obtained results were subsequently analysed using STRESS.Net software, provided by the manufacturer of the machine. Additionally, microhardness measurements were conducted using a Vickers hardness indenter with a load of 200 g and a dwell time of 60 s. The results were averaged from 50 measurements taken at the centre of the specimens.

2.3. Microstructural characterization

Detailed microstructural analysis was performed on the specimens before and after electrochemical polarization experiments. Pore analysis was done on images taken by Leica DMRE optical microscope with magnifications of 5, 10, and 20X (10 pictures from each magnification). The as-built specimens underwent microstructural characterization using various analytical instruments. The FEI QUANTA 250 field emission scanning electron microscope (FE-SEM), equipped with an AMETEK electron backscatter detector (EBSD), was employed. Additionally, the Zeiss EVO MA10 scanning electron microscope (SEM) with Oxford instruments INCAx-act energy dispersive X-Ray Spectroscopy (EDS) capabilities, and the JEOL JSM-7100F FE-SEM were utilized for further analysis.

EBSD maps were taken both in as-received condition and after tensile straining (10 % higher than the yield stress) of the specimens to elucidate the effect of tensile straining on the grains and subgrains misorientation angle. The surface area with the dimension of $10 \times 10\ \mu m^2$ was scanned at 20 kV with a probe current of 10 nA, and a working distance of 10 mm along the longitudinal direction of the specimens, with a step size of 40 nm. The specimens were polished up to 50 nm colloidal silica suspension following standard metallographic sample preparation prior to EBSD measurements. For each type specimen, five different regions were analysed by EBSD in order to have a clear idea regarding the average misorientation angle variation between the mentioned specimens. All post-processing of the EBSD results was done utilizing OIM analysis and MTEX toolbox.

Microstructural analysis on as-built specimens was performed by etching the specimens with Kalling's 2 reagent (2 g $CuCl_2$, 40 ml HCl, 8 ml Ethanol). Subgrain width analysis was performed on the etched surface of the specimens, by taking 5 random SEM pictures with a magnification of 10000X at 15 KeV. 1500 subgrain measurements were performed for having a good statistical analysis from various sites. Moreover, EDS compositional mapping was performed on various specimens in order to shed light on the micro segregation state of alloying elements within laser tracks and pore sites. Furthermore, Transmission Electron Microscopy (TEM) analysis was conducted using a FEI Tecnai G2 F20 instrument (Field Electron and Ion Company, USA) operating at 100 kV. TEM samples were prepared by manual grinding to a thickness of up to 70 μm, followed by electrochemical polishing using a STRUERS TENUPOL-3 twin-jet polishing unit. The polishing process employed a solution containing 95 % acetic acid and 5 % perchloric acid, with a voltage of 45 V at −25 °Celsius. The specimens were examined after electrochemical polarization experiments to investigate the corrosion morphology and potential surface crack initiation mechanisms using high-magnification FE-SEM analysis. All image analysis was performed employing ImageJ software [36].

2.4. Scanning Kelvin probe force microscopy (SKPFM) analysis

Scanning Kelvin Probe Force Microscopy (SKPFM) was employed utilizing a Park Systems XE–100 atomic force microscope. The measurements involved the use of rectangular conductive cantilevers (ANSCM–PT from AppNano) with a Pt/Ir coating, a resonant frequency ranging from 50 to 70 kHz, and a spring constant between 1 and 5 N/m. The analysis employed a dynamic mode with a single-pass approach, enabling the simultaneous acquisition of topography and corresponding potential images. The obtained potential signal, known as the contact potential difference (CPD) between the tip and the sample, reflected the variation between the work function of the probe and the surface [37, 38]. Furthermore, to accurately represent the relationship between the Volta-potential values of the investigated surface, the recorded potential signal was inverted.

The SKPFM measurements were conducted in all the samples (one sample after the other), and after finishing the analysis of the last specimen, the first sample was measured again. This was done to ensure

that the volta potential of the AFM probe did not change due to wear, geometrical changes of the tip apex, or contamination [39]. Since the same CPD value was obtained in the second scanning of the initial sample analysed, this confirmed that no damage occurred on the AFM probe used, but also allowed the direct comparison of the CPD values obtained on the different samples. These CPD values are the Volta potential difference between the samples' surface and the AFM probe. Given that no variation occurred in the Volta potential of the probe, variations between the measured CPD represent variations in the Volta potential of the different specimens analysed.

2.5. Electrochemical polarization response and surface cracking characterization

It is well recognized that incubation and initiation of cracks take place in extremely localized sites, which makes the detection and further analysis of the initiation mechanisms quite challenging [40]. In authors' previous investigations implementing the microcapillary method [35,41], it has been shown that the method has the potential to analyse the crack initiation susceptibility of austenitic alloys and could be used for in-depth characterization of the cracking mechanism, with high repeatability of the results. It is worth mentioning that the microcapillary technique had been implemented by Breimesser et al. [32] and the comparability of the results with conventional methods had been evaluated in various investigations in the past decade. The use of microcapillary technique improves significantly the precision and resolution of the detection of such very small alterations in current density and potential during the incubation/initiation of SCC. These subtle alterations often remain undetectable using conventional polarization techniques, as a consequence of higher surface areas in contact with the solution.

Electrochemical polarization experiments were performed in two conditions, as-built and under constant tensile straining corresponding to 10 % higher than the yield strength for each specimen. The choice of such a strain level is based on historical test methods employed for SCC susceptibility studies of nickel-based superalloys in BWR and PWR in an accelerated manner [12,40]. Tensile straining on the specimens was precisely measured by DT9829 high precision mixed sensor USB device (Measurement Computing Corporation, USA) combined with strain gauges, implementing a half Wheatstone bridge configuration in order to enhance the repeatability of the applied strain. For the comparative study, a 3.5 % sodium chloride solution in distilled and deionized water was selected as the testing solution. Prior to the measurements, the solution was bubbled with argon gas for 5 min. This step was taken to achieve the same dissolved oxygen level, which significantly enhances measurement repeatability within the self-controlled conditions of the microcapillary technique. An electrochemical setup utilizing the standard three-electrode method was employed. The reference electrode used was a standard calomel electrode (SCE), while a platinum wire with a diameter of 0.3 mm served as the counter electrode. A Gamry Interface 1010E potentiostat unit from Gamry Instruments (USA) was utilized for the electrochemical measurements. A capillary tip, with a diameter of 500 μm, was employed while maintaining a distance of 3 mm between the platinum counter electrode and the surface. To enhance measurement accuracy and mitigate the risk of crevice corrosion, a thin layer of silicon-based gasket was applied to the tip of the capillary.

Potentiodynamic polarization measurements served as the initial step in comprehending the overall corrosion response and determining the precise parameters for subsequent experiments. The measurements involved scanning the potential within the range of −0.5 to 1.5 mV relative to the open circuit potential (OCP). The OCP was measured for a duration of 60 min prior to the potentiodynamic polarization experiments for all specimens. The scan rate used for potentiodynamic polarization experiments was 2 $mV.s^{-1}$.

Galvanostatic polarization experiments were conducted for a limited period of time of 1000 s and keeping the current density at a constant value corresponding to 10 % higher than the current density at the breakdown potential acquired from potentiodynamic polarization measurements. Since the current density was kept at a value relatively close to the passive current density, very limited corrosion is expected to occur on the exposed surface area. Such a method could provide tremendous information regarding the resistance of the native passive layer to localized types of corrosion such as pitting and/or SCC initiation in an accelerated manner while avoiding significant alteration of the water chemistry due to the limited current density and exposure time.

Furthermore, to investigate the influence of microstructural variations on the evolution of the native oxide layer, potentiostatic experiments were conducted within the passive region of the specimens, which were previously obtained from potentiodynamic polarization experiments. The potentiostatic measurements involved maintaining a constant potential at 10 % lower than the breakdown potential. Prior to the actual measurements, the specimens were allowed to remain in contact with the solution for 30 min. Each measurement was performed at least three times to enhance precision, repeatability, and ensure the reliability of the reported results. To ensure that no crevice corrosion occurred during the electrochemical polarization experiments, all the specimens were checked with SEM after the tests.

3. Results

3.1. Mechanical and microstructural characterization

Obtained hardness results indicated a meaningful trend with the variation of laser power. As shown in Fig. 2a, the mean value of the hardness slightly increases from 345 HV for the specimen with a laser power of 105 W to a value of 356 HV for 115 W samples, followed by a more substantial decrease to 318 HV for the case of 125 W samples. The yield strength value of the specimens was 725 MPa for 115 W case, as reported in our previous study [35], and specimens with various laser powers indicated a minor variation of ±30 MPa compared to 115 W specimen. To ensure that the yield strength of all specimens used for electrochemical polarization and stress-assisted crack initiation experiments presented the same value, the permanent plastic deformation after tensile straining of the specimens was measured. The results indicated a minor variation of around 1 % in the measured elongation for all specimens, highlighting almost identical condition irrespective of short-range variation of laser power. Furthermore, X-ray diffraction residual stress measurements suggested a minor increase in tensile residual stress magnitude with an increase in laser power with the values of 108±9, 124±6, and 159±8 MPa for the specimens of 105, 115, and 125 W, respectively.

It is important to mention that the process parameters and laser power range used for the fabrication of the specimens were intentionally chosen to have the highest density with slight variations to reflect the microstructural alterations more willingly (having the same defect types). The surface porosity coverage of the specimens was estimated by dividing the total pores surface area by the total analysed surface area. This indicated a slight variation with an increase in laser power (as seen in Fig. 2b). The measured density was 98.8, 99.6, and 98.4 % for specimens 105, 115, and 125 W, respectively, demonstrating the optimum range of laser power for obtaining the highest density for alloy 718. The difference in pore surface area between specimens with laser power of 105 and 115 W was not significant, representing a slightly lower value for the 115 W case. A more substantial increase in porosity was observed for 125 W specimens, highlighting a noteworthy correlation of laser power (higher than a threshold) with size and distribution of the defects present in L-PBF fabricated specimens of alloy 718. In terms of pore morphology, the pores exhibited a spherical shape in all specimens, indicating the presence of gas pores. Notably, specimens fabricated with a laser power of 125 W exhibited an increase in both pore density and size. The total number of detected pores was 743, 558, and 1093 for specimens processed at laser powers of 105 W, 115 W, and 125 W,

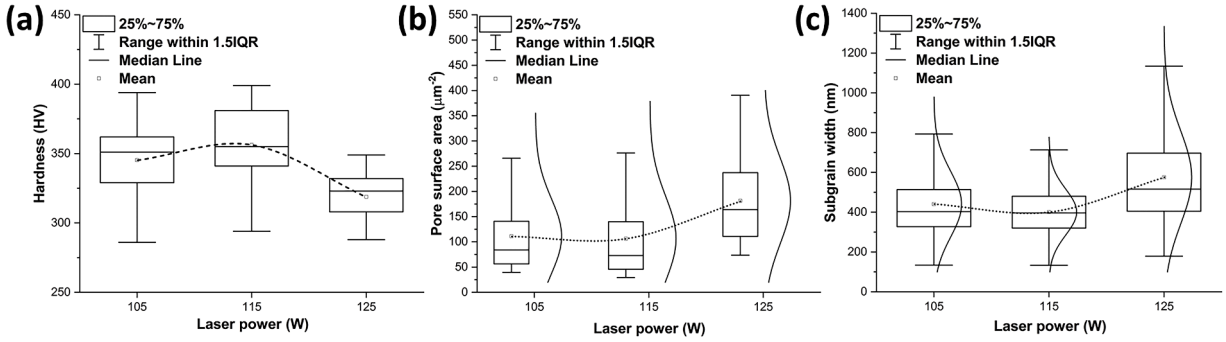

Fig. 2. (a) Vickers hardness, (b) pore surface area, and (c) width of subgranular structure variation with laser power.

respectively. Similarly, subgrain width revealed a correlation with laser power as well. As shown in Fig. 2c, subgrain width slightly decreases with an increase in laser power from 105 to 115 W, followed by an increase with a further increase in laser power. Furthermore, microstructural analysis of the specimens with various laser powers (Fig. 3), highlighted the overall austenitic matrix with the presence of non-equilibrium phases at subgrain boundaries.

3.2. TEM analysis of as-built state

TEM analysis was conducted to enlighten the submicron structural variations with an increase in laser power. As shown in Fig. 4, high density and entanglement of dislocations in the close vicinity of the subgrain boundaries are observed for all cases. Surprisingly, a substantial increase in dislocation density can be clearly seen for the 125 W case (Fig. 4c, d) compared to the samples prepared using other laser powers.

It must be emphasized that generally, dislocations at the subgrain scale are case-sensitive and could change substantially from one zone to another. Thus, for all specimens, a minimum of 10 pictures, randomly taken from the TEM sample, were analysed and compared for qualitative analysis of dislocation density, and representative pictures are reported herein. Furthermore, submicron carbide particles and nano cavities, mostly located at subgrain boundaries, were also detected for all cases (Figs. 5, and 6). More in-depth analysis of the melt pool boundaries (MPB), which the same nomenclature is used for laser track boundaries herein, and grain boundaries are shown in Fig. 5, revealing the presence of high dislocation density at MPBs and distortion of some subgrains (with a high density of stack faults, thickness fringes, and other defect types) at the interface of adjacent melt pools (Fig. 5a). In addition, to a lesser extent, the same dislocation entanglement and distortion of subgrains were detected for the grain boundaries (Fig. 5b), highlighting a noticeably higher magnitude of submicron plastic strains at such places. Moreover, analysis of the subgrain boundaries with higher magnification (Fig. 6), further elucidated the presence of nano cavities at subgrain boundaries, combined with nano-sized carbides (with larger size compared to cavities), emphasizing high dislocation density adjacent to

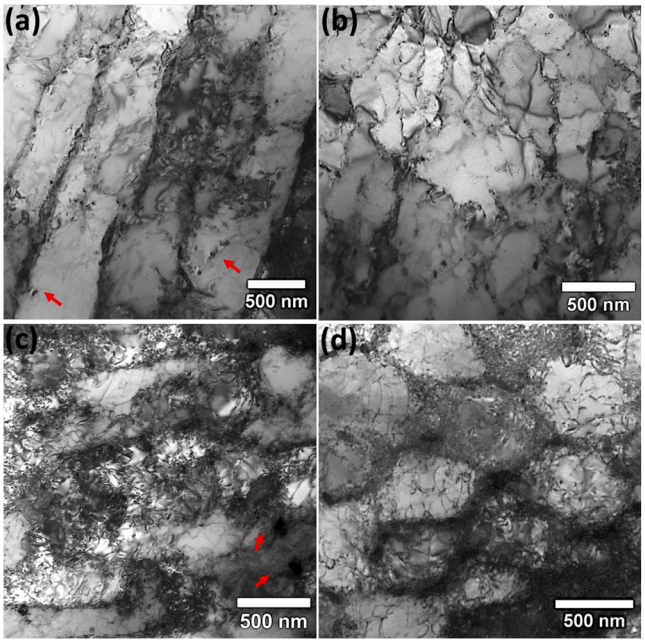

Fig. 4. TEM analysis of the specimens in the as-built state for (a) 105 W, (b) 115 W, and (c, d) 125 W cases. The submicron structure consists of carbide particles shown by red arrows.

carbide phases. From the analysis of the size and density of such particles, it can be stated that the size of carbides and the distribution of nano cavities increased with an increase in laser power.

The most remarkable result to emerge from the TEM analysis is the presence of a meaningful direct correlation between dislocation density, submicron carbides distribution, and nano cavities adjacent to subgrain boundaries, with laser power of the L-PBF process. This stresses the

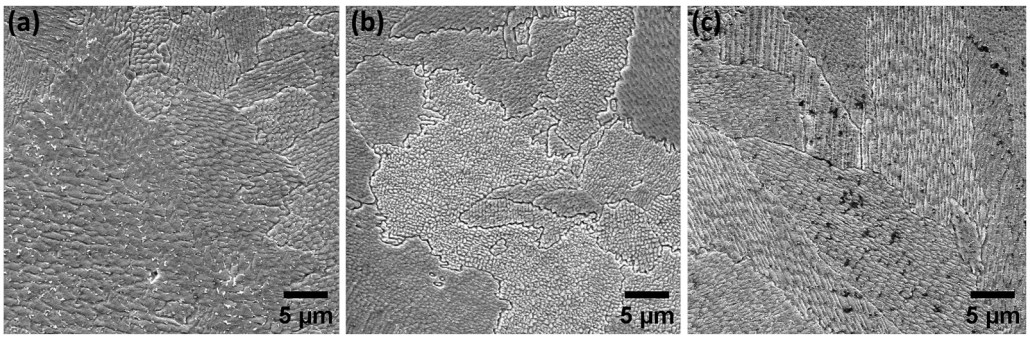

Fig. 3. As-built microstructure of (a) 105, (b) 115, and (c) 125 W specimens after etching.

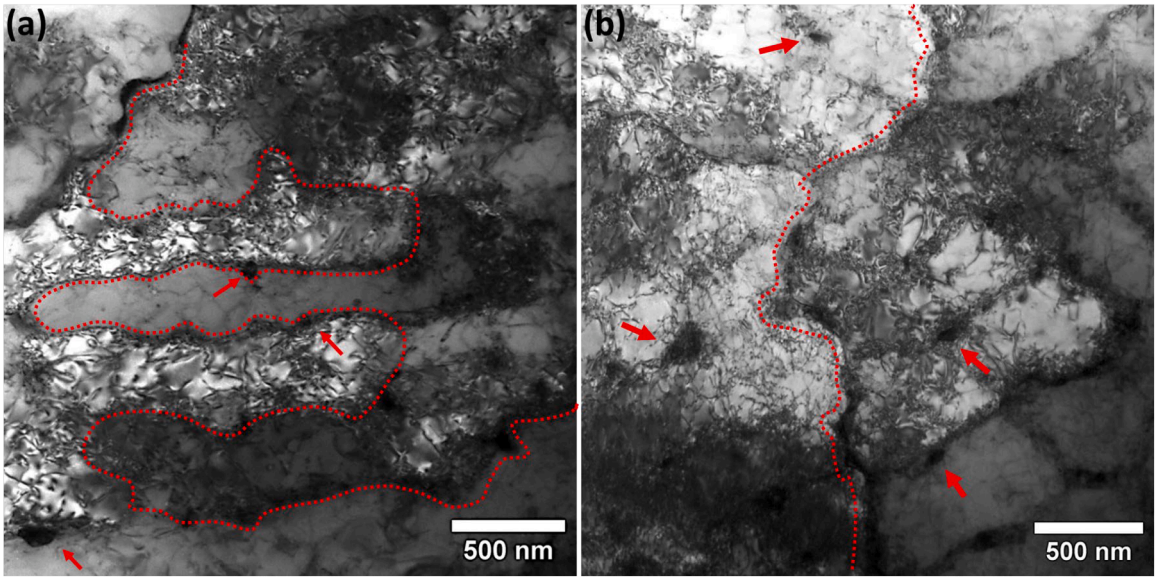

Fig. 5. TEM analysis of (a) a region at a melt pool boundary, and (b) grain boundaries of the specimen with a laser power of 125 W (shown by dashed red lines). The submicron structure consists of carbide particles shown by red arrows.

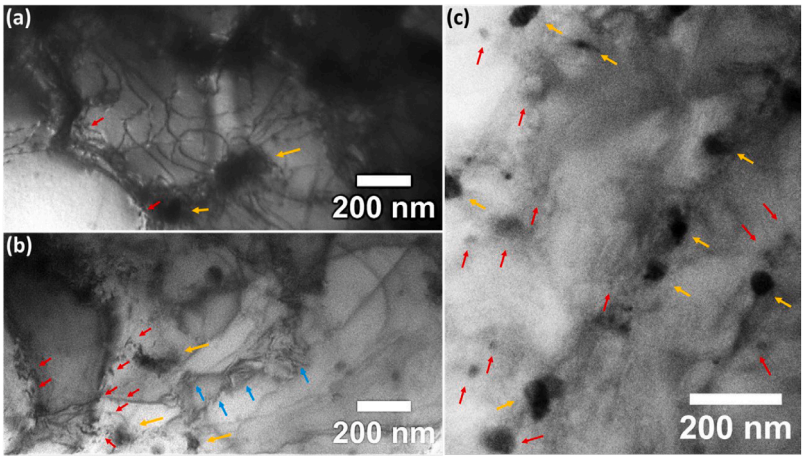

Fig. 6. High magnification analysis of the nanocavities (shown with red arrows), precipitates (shown by yellow) arrows, and stack faults highlighted by blue arrows. (a) specimen with laser power of 115 W, and (b, c) 125 W with different magnification from various sites.

importance/impact of short-range variations in process parameters on submicron characteristics of the fabricated components, which could potentially alter the electrochemical behaviour and surface cracking susceptibility. It is worth mentioning that the detection of various phases and nanocavities observed in TEM images was confirmed/supported by the analysis of their corresponding diffraction patterns obtained from each phase and by comparing the results with the diffraction patterns simulated by implementing CrysTBox [42] software (data not shown herein).

3.3. Crystallographic orientation in as-built, and tensile-strained conditions

Inverse pole figures (IPF) acquired in the loading direction (XY plane), with the Z axis parallel to the build direction, and the corresponding kernel average misorientation (KAM) are shown in Figs. 7 and 8, for the specimens with various laser powers in both as-built and tensile strained states.

As can be seen from the analysis of the IPF, the variation in structure and crystallographic orientation indicated minor difference. Even after tensile straining the difference was not considerable between specimens. On the other hand, KAM analysis of the specimens before and after tensile straining (Fig. 8) indicates a high density of low-angle misorientations (less than one degree) in all cases, revealing a slight increase in misorientation angles for all specimens after tensile straining compared to as-built condition, with a higher increase for the case of 125 W specimens. However, the measured KAM for all cases was less than 2°, highlighting low sensitivity of the microstructure in grain scale to tensile straining. Although the difference in KAM was not major between the different samples, it might be stated that the misorientation angle was slightly lower for the case of 115 W compared to the other specimens both at the highest Gaussian distribution and the maximum angle. Furthermore, analysis of the misorientation angle between tensile strained and as-built states (Fig. 8g, and h) highlighted similar trend in misorientation angle variation with changes in laser power.

3.4. SKPFM analysis

To investigate the impact of short-range variation in laser power on the surface condition, SKPFM analysis was performed on the specimens.

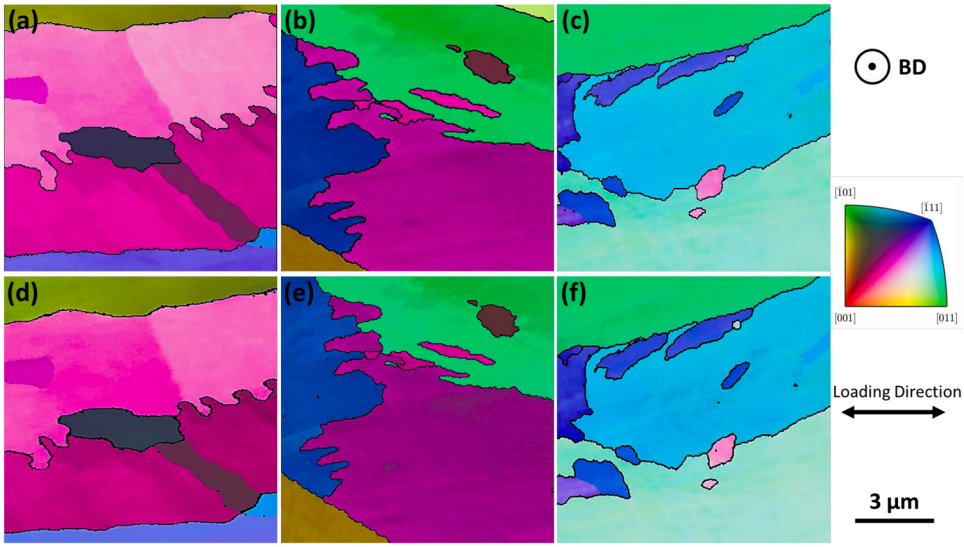

Fig. 7. Inverse pole figure (IPF) maps in as-built state for (a) 105 W, (b) 115 W, (c) 125 W, and in tensile strained state for (d) 105 W, (e) 115 W, and (f) 125 W.

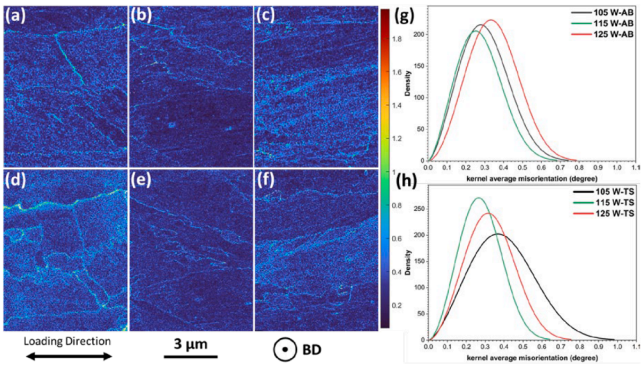

Fig. 8. KAM analysis of in as-built state for (a) 105 W, (b) 115 W, (c) 125 W, and in tensile strained state for (d) 105 W, (e) 115 W, and (f) 125 W, with statistical distribution (g) in as-built, and (h) tensile strained state corresponding to IPF maps shown in Fig. 8. (AB) corresponding to as-built state, and (TS) corresponding to tensile-strained state.

Fig. 9 illustrates an example of the topography and Volta potential map obtained from the surface of the specimen fabricated with a laser power of 115 W. The Volta potential maps obtained through SKPFM (Fig. 9b) illustrate the surface potential relative to the metal probe, known as the CPD. The measured CPD values obtained through SKPFM exhibit a direct correlation with the work function of the specimen, thereby providing insights into the surface condition of the sample. A lower work function value signifies heightened electron activity at the material's surface, which can potentially result in an elevated corrosion rate.

In contrast, a higher work function is frequently linked to improved resistance against corrosion. When a metal or alloy is shielded by a thin native oxide layer, the work function becomes closely intertwined with the characteristics of this oxide film, such as its thickness and noble properties [43]. Thicker oxide layers, which offer enhanced protection, lead to higher CPD values. The surface potential of the specimens, as observed in Fig. 9b, displays a relatively uniform distribution owing to the microstructural refinement achieved through the rapid solidification process intrinsic to the manufacturing technique. In order to investigate the impact of laser power on the surface CPD condition, a statistical analysis was conducted on the collected data, encompassing measurements taken at various regions and resolutions. As depicted in Fig. 10a, the CPD values for specimens fabricated with laser powers of 105 W and 115 W exhibit remarkable similarity. However, the surface potential of the 105 W specimen consistently exhibits a slightly higher value compared to the 115 W specimen. This decrease in surface potential becomes more pronounced when examining the sample fabricated with

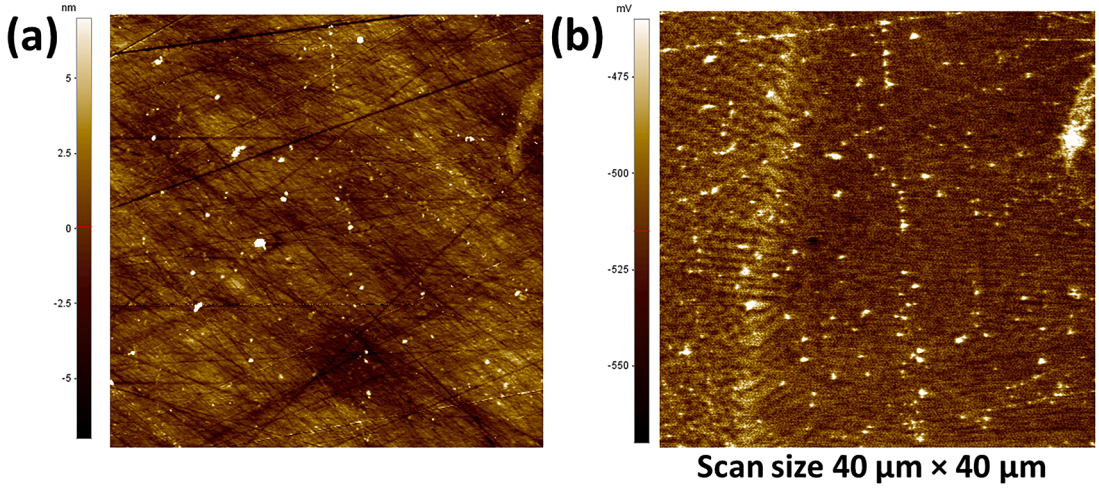

Fig. 9. Representative (a) topography and (b) potential (CPD) map obtained by SKPFM.

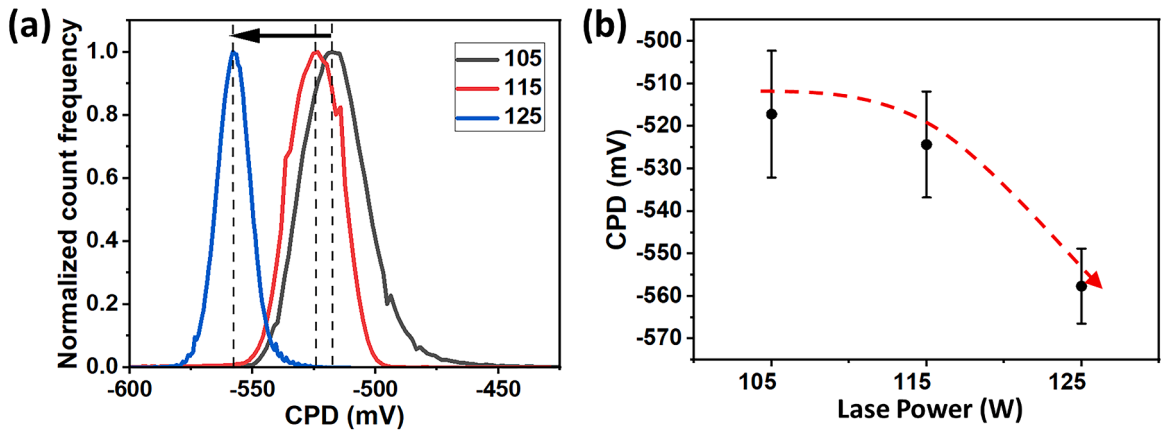

Fig. 10. (a) Histograms of CPD maps obtained by SKPFM on the different samples, and (b) correlation of average CPD potential with laser power.

a laser power of 125 W. Furthermore, the potential distribution shape (Fig. 10a) demonstrates symmetry across all cases, affirming a relatively homogeneous microstructure at the microscale, irrespective of laser power. The trend in CPD values for specimens with varying laser powers is summarized in Fig. 10b, clearly indicating a significantly lower potential (less noble) for the 125 W specimen in comparison to the others. Notably, the calculated nanoscale surface roughness (Ra) of the specimens derived from AFM images ranged from 1 to 1.7 nm, indicating very low values. Consequently, it can be confidently asserted that the SKPFM results were primarily influenced by underlying microstructural features rather than variations in surface roughness.

3.5. *Electrochemical polarization results*

Potentiodynamic polarization experiments were conducted on as-built as well as tensile-strained specimens and the results are summarized in Table 2. Results obtained for both as-built and tensile strained conditions (Fig. 11a) highlight low sensitivity of corrosion potential (E_{corr}) and current density (I_{corr}) to laser power variation. Considering the breakdown potential (E_{break}) and current density (I_{break}) in the as-built state, a minor reduction in E_{break} was detected with an increase in laser power from 105 to 115 W, followed by a more considerable decrease with a further increase in the laser power to 125 W. After tensile straining the specimens, potentiodynamic results indicated a decrease in breakdown potential for all cases. However, the decrease was less noticeable for the specimens of 105 and 115 W, highlighting higher resistance to localized corrosion attack.

On the other hand, specimens with a laser power of 125 W, revealed significantly lower localized corrosion resistance and a substantial decrease in E_{break} after tensile straining, compared to the as-built state. Interestingly, results after tensile straining of the specimens revealed an increase in I_{break} for 105 W and a more significant increase for the case of 125 W specimens. Nevertheless, for the case of 115 W, the variation in I_{break} was insignificant compared to other cases, suggesting higher localized corrosion resistance of the 115 W sample even after tensile straining.

The microcapillary galvanostatic polarization results, as shown in (Fig. 11b), revealed in more detail the correlation of laser power variation with localized corrosion resistance. Considering the as-built state, 115 W specimens indicated higher maximum potential and substantially prolonged duration before the sudden potential drop compared to 105 and 125 W cases. Specimens with a laser power of 125 W showed both the least potential and duration, highlighting drastically lower resistance of the passive layer to the localized breakdown in the as-built state. Likewise, results after tensile straining of the specimens revealed a more considerable decrease both in maximum detected potential and duration before the potential drop for 125 W specimens compared to 105, and 115 W, which presented a less evident decrease between as-built and tensile loaded states. From the galvanostatic polarization results, it could be stated that the specimens with a laser power of 115 W obtained superior resistance of the passive layer to localized forms of corrosion, compared to other specimens. Results from galvanostatic measurements are summarized in Table 2.

Furthermore, potentiostatic polarization results, performed in potentials 10 % lower than the E_{break} are summarized in Fig. 11c. Likewise, specimens with a laser power of 115 W obtained the lowest current density, while specimens of 105, and 125 W presented significantly higher current density by the order of almost two times more. Potentiostatic results confirmed the previous observations for the superior resistance of the passive layer for the 115 W specimens even in a tensile strained state, showing less current density compared to other cases. It is worth mentioning that although the 115 W specimens were the most resistant ones in both as-built and tensile strained conditions, current density increased significantly for all specimens after tensile straining compared to the as-built state, highlighting the advantage of using microcapillary electrochemical polarization methods in the detection of SCC activity during the stress state of the specimens.

A remarkable result to emerge from the electrochemical polarization measurements utilizing the microcapillary technique is that the method is a straightforward technique in the quantitative and comparative study

Table 2
Summary of electrochemical polarization results for (AB) as-built, and (TS) tensile strained states.

State	Laser Power (W)	Potentiodynamic (E-I)				Galvanostatic ($I_{constant}$)		Potentiostatic ($E_{constant}$)
		E_{corr} (mV_{SCE})	I_{corr} ($mA.mm^{-2}$)	E_{break} (mV_{SCE})	I_{break} ($mA.mm^{-2}$)	E_{drop} (mV_{SCE})	t_{drop} (s)	I_{std} ($mA.mm^{-2}$)
AB	105	−586.19	4.63E-6	671.15	4.77E-4	767.51	208	9.63E-4
	115	−621.83	6.19E-6	658.14	5.25E-4	791.31	331	6.06E-4
	125	−595.81	9.11E-6	521.83	3.41E-4	736.11	174	1.10E-3
TS	105	−553.95	8.07E-6	645.13	7.02E-4	751.64	179	1.11E-3
	115	−634.84	6.03E-6	641.74	5.85E-4	771.65	274	1.04E-3
	125	−602.60	7.70E-6	447.27	7.93E-4	498.04	54	1.29E-3

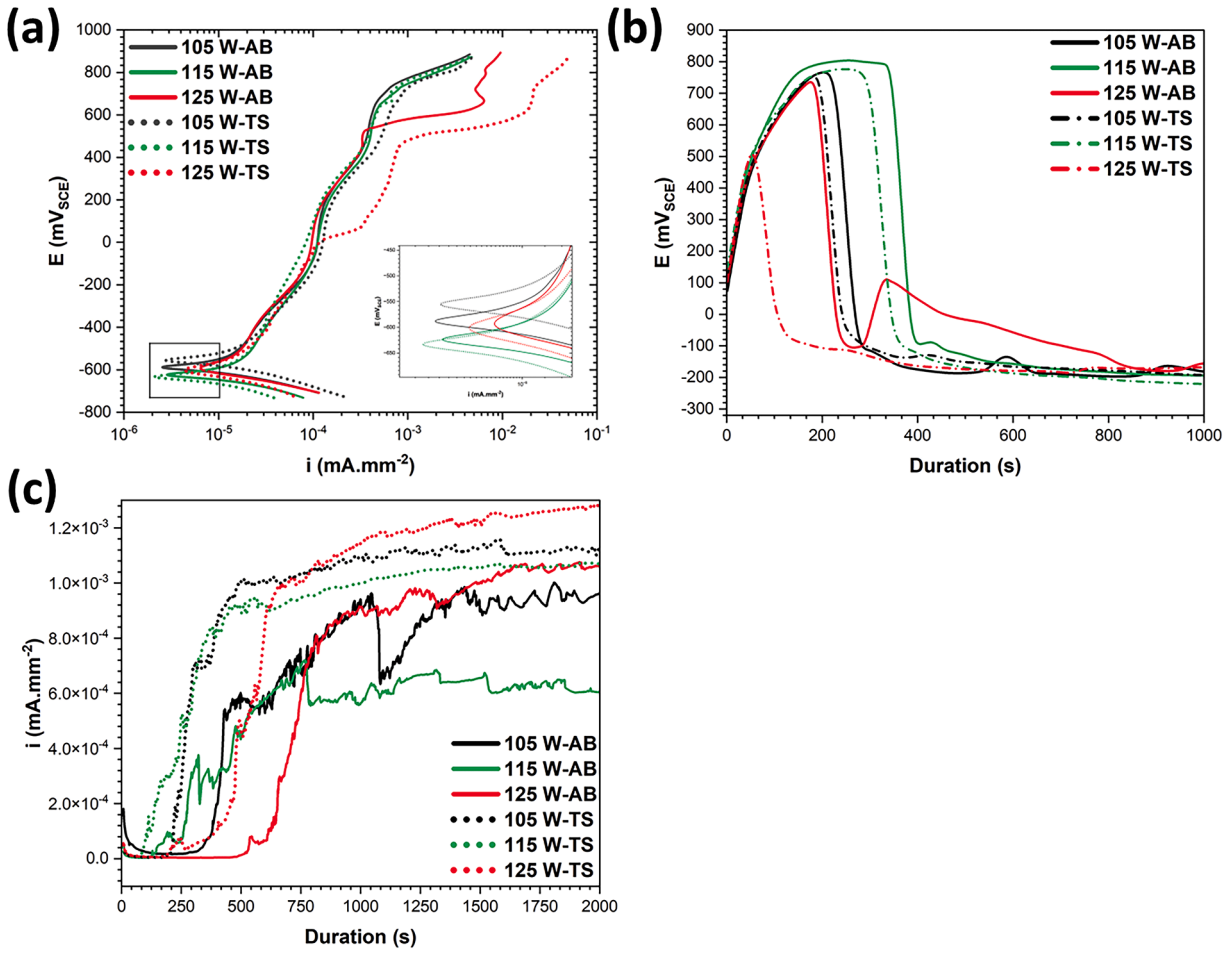

Fig. 11. (a) potentiodynamic, (b) galvanostatic, and (c) potentiostatic polarization results for the specimens with the variation of laser power in as-built (AB), and tensile-strained (TS) states.

of even slight variations in microstructural alterations and the possibility for the detection of early stages of corrosion activity in defects such as pits and initiated cracks by in-depth analysis of potential and current density variations over time of exposure.

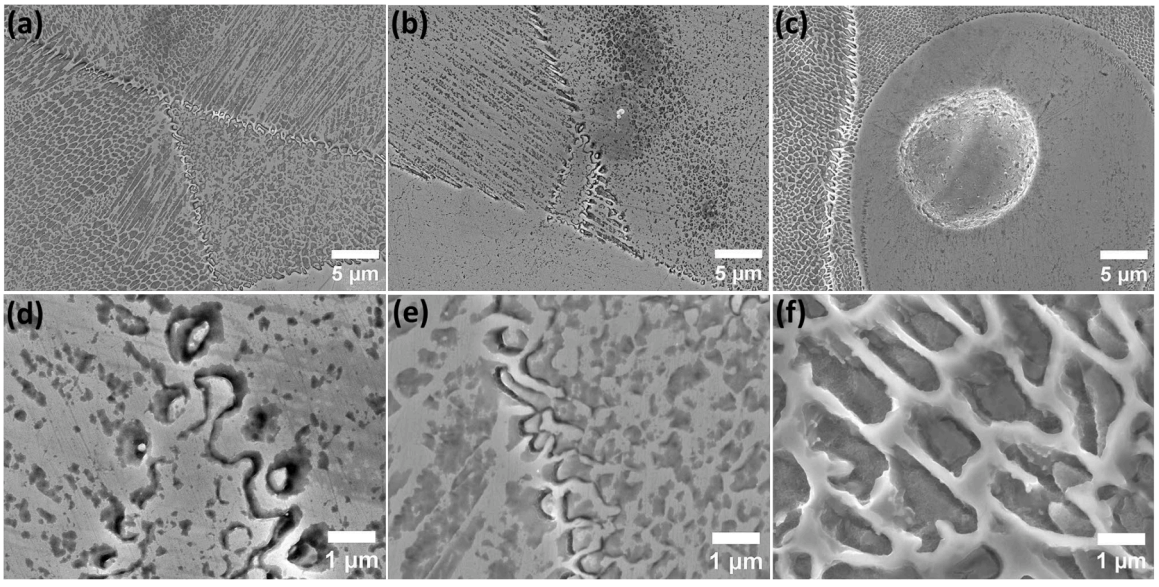

Fig. 12. Corrosion attack morphology after galvanostatic test for the as-built state of (a, d) specimen 105 W, (b, e) specimen 115 W, and (c, f) specimen 125 W at various magnifications.

3.6. Corrosion morphology and initial stages of cracking

Scanning Electron Microscopy (SEM) was utilized to examine the morphology of corrosion attacks and the severity of surface crack initiation in both the as-built and tensile strained states. This analysis was performed on the samples subjected to galvanostatic tests. As depicted in Fig. 12, the as-built state primarily exhibited selective dissolution of the subgrain austenitic matrix, while the subgrain boundaries remained intact. Notably, the selective dissolution attack was significantly more severe in the 125 W specimen compared to the specimens fabricated with 105 W and 115 W, which displayed similar corrosion morphology and attack severity. Furthermore, the MPBs were more severely affected in all cases compared to the interior of the melt pools. Overall, the analysis of the specimens in the as-built state emphasized that the residual stresses in this condition were insufficient to trigger crack initiation. The round region in Fig. 12c is a section of a gas pore. This is not corroded (as with most pores seen during SEM analysis), which confirms that the role of porosity in the electrochemical responses obtained was minimal.

The condition changes significantly after tensile straining of the specimens (Fig. 13), revealing the initiation of surface cracks for all cases. Crack initiation was clearly less severe for the case of 115 W compared to 105 W and 125 W specimens. For the 115 W case (Fig. 13b), a higher tendency to the selective dissolution of the subgrain matrix than crack initiation was observed, highlighting less noticeable alteration in tensile strained compared to the as-built state.

However, shallow cracks at the surface were still detected, which could be the cracking of the corrosion products and/or oxides formed on the surface during the electrochemical polarization experiment (Fig. 14b). For the case of 125 W and 105 W specimens (Fig. 14a, c) the cracks initiated seem to be much deeper than those seen on the sample fabricated at 115 W. This suggested that some of these cracks might propagate beyond the thickness of the oxide/corrosion product layer. Moreover, the severity of crack initiation, by means of the crack mouth opening, is more pronounced for the case of 125 W specimens (Fig. 14c), suggesting faster initiation kinetics and more time for crack growth compared to the other two samples. Interestingly, cracks were mostly initiated from the close vicinity of subgrain boundaries, revealing a preferential site for surface cracks initiation for the case of L-PBF 718. Additionally, high-resolution FE-SEM analysis of crack initiation sites (Fig. 14) on tensile strained specimens reveals the complete debonding of the austenitic subgrain matrix from the subgrain boundaries. Furthermore, selective dissolution of the austenitic matrix was also detected at subgrains, highlighting the synergistic and complex effect of various factors involved in the initiation of these cracks.

4. Discussion

To develop a comprehensive understanding of how laser power influences the extent of selective dissolution of the subgrain matrix in the as-built state, it is crucial to elucidate the underlying mechanism driving this selective dissolution. Elemental segregation towards the subgrain boundaries (cell walls) establishes a galvanic coupling between the subgrain matrix and these boundaries in the presence of an electrolyte, regardless of the laser power employed. Consequently, the necessary conditions for selective corrosion to occur at the coupled environment formed between the subgrain matrix and boundaries are readily present. This has already been proposed/discussed in our previous work [35].

This work demonstrated that slight variations in laser power (laser energy input) during additive manufacturing cause microstructural variations that can considerably alter the corrosion resistance and susceptibility of the material to surface cracking under straining conditions. Experimental results revealed that an increase in laser power led to microstructural alterations such as a consequential decrease in hardness magnitude, an increase in pore size and density, an increase in subgrain width, a significant increase in dislocation and nanocavities densities at subgrain boundaries, and significantly less noble surface potential.

With an increase in laser power, a series of important alterations such as an increase in the maximum temperature of the melt pool [44,45], thermal gradient [44,46], solidification duration [46], molten pool length [46,47], and decrease in melt viscosity, depending on the thermal conductivity of the material [44,47,48], could readily occur. Furthermore, variations in laser power and in general energy input density could affect the crystal orientation and subgrain structure from cellular to dendritic, as extensively investigated by Gokcekaya et al. [49]. This work indicated the transition to crystallographic lamellar microstructure (CLM) or single-crystal-like microstructure (SCM) with an increase in laser power. Such microstructural alterations are reported to be responsible for better mechanical properties for the CLM microstructure compared to SCM. Furthermore, from the TEM analysis presented herein, it is clear that such thermal alterations with an increase in laser power (and in general, energy density input), combined with an increase in thermal shrinkage [50], led to an increase in dislocation density, nanocavities (formed as a consequence of higher shrinkage), and wider subgrains.

In general, SCC initiation events are closely linked with the integrity of the passive layer. The native oxide layer present on the surface of Ni-Fe-Cr-based alloys serves as a barrier, impeding electron mobility across the surface in contact with the solution. Potentiodynamic polarization techniques, while useful, fall short in comprehensively tracking the evolution of this native oxide layer over time. To delve deeper into the temporal evolution of passive layer integrity under accelerated exposure conditions, galvanostatic and potentiostatic experiments were conducted at critical conditions, as detailed in this manuscript.

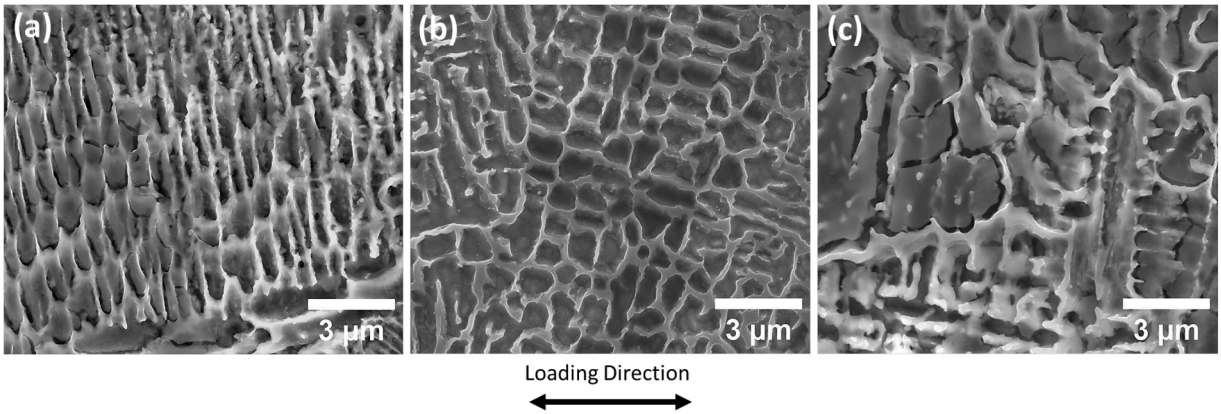

Fig. 13. . Crack initiation after tensile straining of the (a) 105 W, (b) 115 W, and (c) 125 W specimens at different magnifications. .

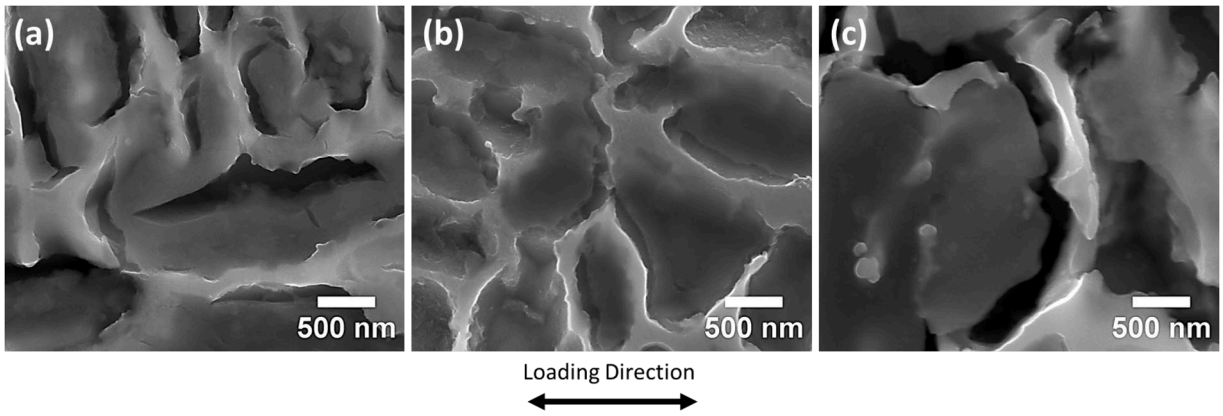

Fig. 14. High-resolution FE-SEM images of crack initiation morphology for (a) 105 W, (b) 115 W, and (c) 125 W specimens after tensile straining.

Concerning the galvanostatic polarization experiments, the native oxide layer resists to the free movement of electrons until the moment there is a local dissolution/destruction (as is the nature of materials with native oxide layers, instead of general corrosion occurrence). Before local breakdown of the passive layer, the potential values recorded are relatively high, highlighting the resistance of the passive layer. When the balance between the destruction and formation of the passive layer cannot be hold anymore, the relatively higher dissolution rate (as a consequence of various microstructural and environmental factors such as the accumulation of ions on the interface of the materials with the solution) leads to the breakdown of the passive layer, and therefore easy transfer of electrons, leading to a sudden potential drop. Considering Ohm's law, the maintenance of a constant current density in galvanostatic measurements signifies that elevated potential values equate to greater resistance within the passive layer. Consequently, tracking the evolution of potential over exposure time offers extensive insights into passive layer integrity and discrepancies in the overall behaviour across distinct samples. This critical juncture, marked by an abrupt potential decline, aligns with the onset of localized corrosion attacks, including pitting, crevice formation, and/or SCC initiation.

Similarly, in potentiostatic tests, a similar reasoning applies. Until the passive layer approaches critical conditions leading to breakdown, the current passing through the passive film remains relatively low. Upon reaching the threshold for passive layer breakdown, a sudden increase in current becomes evident. Unlike galvanostatic measurements, potentiostatic polarization experiments do not restrict current flow, allowing for insightful data acquisition from post-passive layer breakdown. This information can unveil the kinetics of material dissolution, offering a robust tool for comparative analysis among diverse materials.

Concerning the impact of laser power on the corrosion performance of the materials, several links can be established between the microstructural variations observed and the corrosion behaviour of the samples. First, the higher pitting corrosion resistance of specimens fabricated at 115 and 105 W compared to 125 W samples can be related to the finer subgranular structure and relatively lower density of dislocations of those specimens (115 and 105 W) compared to the specimen at 125 W. A finer micro-segregation structure can promote the formation of a less defective, thicker, and therefore more protective native oxide layer (as demonstrated in previous studies for additively manufactured austenitic 316 L stainless steel [51]). This was confirmed by the SKPFM analysis (see Fig. 10) in which the specimens with finer subgranular structure (115 and 105 W) showed higher nobility than sample 125 W. Moreover, dislocation density can also play an important role in the surface condition and surface activity of the materials. As suggested by Liu et al. [52], the hindered movement of dislocations at subgrain boundaries, along with the intricate interaction of entangled dislocations within each subgrain, can result in a significant rise in the energy level of these regions. This elevated energy state in zones with higher dislocation density can subsequently lead to a considerable increase in the presence of point defects within the passive layer. Consequently, the surface can exhibit greater activity and diminished resistance against localized corrosion attack. This can explain why the 125 W specimen (which presents relatively higher dislocation density) is more susceptible to pitting corrosion than the other two specimens. And the same reasoning can explain why the 115 W sample presented the highest corrosion resistance.

However, the relationship between dislocation density and SCC initiation within materials featuring passive oxide layers is multifaceted. Lozano-Perez et al. [53] conducted a comprehensive atomic-level investigation into the evolution of native oxide layers, revealing a continuous formation occurring at the metal-oxide interface, exhibiting a direct correlation with the dislocation density within the specimens. Their findings demonstrate that higher dislocation density actively promotes oxide formation at the metal-oxide interface, by increasing oxygen diffusion along quicker pathways facilitated by regions with higher dislocations. As a result, it could be stated that an increase in dislocation density for the specimen of 125 W, could also enhance the integrity of the passive layer before the breakdown.

In the context of the current study, potentiostatic polarization experiments were conducted within the transpassive region, where both formation and destruction reactions concurrently occur. The prolonged duration before passive layer breakdown observed in the 125 W specimen (Fig. 11C) may be attributed to the presence of accelerated diffusion pathways for oxide formation within areas characterized by higher dislocation density. Thus, based on the experimental findings presented herein, it is conceivable that the deleterious effect of dislocation density on SCC initiation takes place only after the equilibrium between formation and destruction reactions is disrupted, favouring toward higher destruction reactions kinetics (induced by factors such as ion accumulation at the oxide-solution interface and other environmental influences during the incubation stage of SCC). After passive layer breakdown (marked by the rapid increase in current density), the equilibrium current density reached is the highest for the 125 W sample and lowest for the 115 W sample. Therefore, this indicates that, although the 125 W sample presented a delayed breakdown during potentiostatic test (possibly due to more favourable oxidation on high-density dislocation areas), once the passivity breakdown is reached, this high dislocation density can have a negative effect by accelerating corrosion and dissolution reactions.

Conversely, the galvanostatic polarization experiments were performed to study the SCC initiation under conditions favouring destruction reactions more willingly. Consequently, this deliberate approach aimed to enhance the visibility of the detrimental impact exerted by increased dislocation density on facilitating SCC initiation. Another observation that further strengthens the proposed correlation of

dislocation density and corrosion resistance of local sites is the higher susceptibility of melt pool boundaries to localized corrosion attack, which was also detected in the authors' previous investigations on L-PBF fabricated alloy 316 L [32–34]. As seen from the TEM analysis of MPBs (Fig. 5), these regions presented significantly higher density of dislocations compared to other sites of the surface, promoting the presence of higher density of point defects at MPBs. However, further comprehensive investigations at the atomic scale are imperative to gain deeper insights into the intricate interplay between dislocation density and SCC initiation.

When examining the corrosion and surface cracking morphology of the materials under tensile loading conditions, it was evident that the cracking occurred preferentially at the interface between the subgranular cells' matrix and the cells' borders, which from the TEM analysis were sites containing a considerably higher density of dislocations. As explained in previous paragraphs, higher density of dislocations could significantly increase the energy state of the subgrain matrix, which under a tensile strained state could lead to two important events: Firstly, places with relatively higher energy states contain a higher density of point defects at such sites, making the region adjacent to subgrain boundaries more vulnerable to passive layer breakdown (as a consequence of the disturbance in the balance between formation and dissolution reactions). Secondly, higher stresses at the interface of cell matrix and the boundaries (resulting from dislocation impediment under external loading), combined with the noncoherent bound between constituent phases, can lead to higher susceptibility of the interface to crack initiation.

Furthermore, as proposed by Shen et al. [54], both intergranular carbides and nanocavities have an important role in the SCC occurrence of alloy 600 at high temperatures and pressures by lowering the stress needed for the mechanical rupture. With the same justification for crack growth presented by Shen et al. [54], it could be stated that intrinsic nanocavities in the close vicinity of subgrain boundaries (Fig. 6), could contribute to the formation of crack initiation sites by virtue of the ease of mechanical rupture as a consequence of lower minimum stress level needed and coalescence. Moreover, a substantial increase in the number and distribution of carbides accumulated at subgrain boundaries with an increase in laser power from 105 to 115 W to 125 w, could be another shred of evidence for the observed higher susceptibility to crack initiation with an increase in laser power. Although the presence of carbides at grain boundaries are beneficial for improved mechanical properties, by acting as pinning sites for grain growth [55], such particles promote the occurrence of localized corrosion attack due to the depletion of chromium close to carbide phases, as confirmed by Tucho et al. [7]. Thus, areas adjacent to carbide particles with high chromium content could potentially be highly prone to localized corrosion attack as a consequence of chromium depletion adjacent to such particles, promoting crack initiation under tensile stresses.

Nonetheless, it is essential to understand that the initiation of stress-corrosion-assisted cracks is widely acknowledged to be influenced by a complex interplay of various microstructural factors. Based on the findings of the present study, it can be asserted that submicron-scale characteristics hold paramount significance in this context. Therefore, further investigation, focusing on even narrower increments in laser power variation, is imperative to uncover the underlying factors contributing to the marginally superior performance of the 115 W sample in comparison to its 105 W counterpart. The observations from the current study suggest that this enhanced performance in the 115 W specimens may be attributed to a slightly reduced subgrain size, facilitating faster kinetics of passive layer formation reactions. This can lead to fewer point defects.

It is important to highlight that the observations of corrosion morphology for the specimens with various laser powers highlighted no significant variation in the activation of pores as active corrosion sites. Furthermore, it is worth emphasizing that in the current investigation, no signs of cracks forming from pores was detected, pointing towards the idea that other microstructural factors such as higher dislocation density and subgrain width are the dominant factors controlling the surface crack initiation susceptibility of L-PBF 718 alloy. Given that the current findings are based on short-range alteration of laser power in the range of full-density specimens with small amounts of gas pores, careful attention must be exercised for other types of pores such as lack of fusion defects, since the mechanisms for the effectiveness of such sites as active corrosion sites are unquestionably different. Furthermore, in light of the nearly identical residual stress state for the samples of 105 W and 115 W, followed by a slight increase for the 125 W specimens, and very close kernel average misorientation angles among specimens subjected to varying laser powers (accounting for measurement errors), it can be asserted that the observed notable changes in crack initiation were more influenced by submicron alterations. However, in a recent investigation, Gokcekaya et al. [56] highlighted the importance of crystallographic orientation on the oxidation behaviour of pure chromium. Hence, it should be emphasized that the current results are valid for the orientation angle alterations within subgrains of L-PBF manufactured specimens of alloy 718 within the laser power range of the current investigation. Moreover, it is well known that residual stresses can have a high impact on crack initiation susceptibility. In this work, although the difference in residual stress is less pronounced between 105 W and 115 W samples (108±9 and 124±6 MPa, respectively), this difference is not insignificant when compared with the 125 W sample (159±8 MPa). The presence of internal residual stresses can, therefore, influence the cracking behaviour of these samples, specially of the 125 W specimen. However, although the 115 W sample presents a slightly higher value of residual stresses than the 105 W specimen, the cracking susceptibility of the 105 W sample was higher than that of the 115 W specimen. This demonstrate that other sub-micron microstructural variations may be playing a dominant role in the observed experimental results. This confirms that the cracking behaviour is a very complex phenomenon, involving several microstructural features.

Furthermore, the cracking of the surface was observed after tensile straining of the specimens and were not detected in as-built state, pointing toward the idea that such initiation sites were formed as the synergistic effect of tensile stresses, corrosive media, and susceptible microstructure, which are the well-known characteristics of SCC. Although the dislocation density is higher in the 115 W sample than in the 105 W sample, the subgrain size in the 105 W sample is larger than that in the 115 W specimen. Finer subgrains might promote the formation of a thicker and less defective passive oxide layer, which increases the pitting corrosion resistance of the material. This has been previously demonstrated for AM 316 L austenitic stainless steel [51]. Moreover, previous studies, also on 316 L stainless steel, have demonstrated that dislocation densities accelerate the oxidation of the material and the formation of oxide precursors ahead of the oxide front, by providing fast diffusion paths for the oxidation as explained previously [53].In the current investigation, the behaviour of the passive layer and susceptibility to surface crack initiation were examined within a potential and current density range that closely approached the breakdown of the native oxide layer. Such an approach can potentially reveal the mechanism of crack initiation before severe corrosion attack on the surface, which is the main objective and novelty of the current investigation. Although the cracks observed in the current work could be mostly propagating through the oxide layer of the specimens (slightly thickened during the polarization of the sample), this does not exclude that some of these crack tips could reach the metal matrix underneath. Furthermore, preliminary results from ongoing high-resolution analysis of crack initiation sites confirmed that the cracking was not limited to the surface oxide but that some crack tips propagated beyond the oxide layer, reaching the matrix adjacent to cell boundaries. Moreover, these surface cracks (especially deeper cracks as those seen on the surface of the 125 W specimen) represent sites where occluded corrosion cell conditions can be readily formed.

It is also important to mention that the microstructure, and

formation and distribution of defects in additively manufactured parts are not only affected by variations in process parameters, but also by many other factors such as scanning strategy, MAM technology used, power source and feedstock characteristics, or even differences in the size and number of pieces fabricated during a single MAM job. All these parameters/factors can prompt differences in the cooling/solidification rates and thermal history during the layers cycle, and therefore affect the microstructure, properties and performance of the AM part in a difficult-to-predict way. This was highlighted in Section 13 of the 2022 White Paper of the World Corrosion Organization and the European Federation of Corrosion as one of the main challenges that the MAM industry faces nowadays [57]. Therefore, while the exact variations and values of laser power presented in this investigation might be, to some extent, specific to this work, this study does highlight/demonstrate that small process parameter variations can greatly affect the microstructural features of the printed part and consequently its corrosion performance and susceptibility to surface crack initiation. This study is the first step towards enhancing our understanding of the effect of slight variations in microstructural characteristics on crack initiation susceptibility. The microcapillary electrochemical techniques utilized in the current investigation have demonstrated that such techniques could be a powerful tool in comparative studies of crack initiation risk assessment.

5. Conclusion

This study provides compelling evidence that even minor variations in process parameters can lead to significant microstructural changes in printed parts, thereby exerting a substantial influence on their corrosion performance and susceptibility to crack initiation. It also confirmed that there exist an optimum range of laser power (process parameters) in which corrosion and crack initiation susceptibility can be kept relatively low. By employing a combination of microcapillary electrochemical techniques and detailed microstructural analysis, the effect of short-range variations in laser power on the corrosion behaviour and surface cracking initiation mechanism of Ni-Fe-Cr alloy 718 produced through L-PBF was elucidated. The key findings of this study can be summarized as follows:

- Laser power variation caused micro and submicron changes, such as wider subgrains, more porosity, dislocations, and nanovoids near subgrain boundaries, as well as carbide particles with the increase in laser power. Hardness and surface nobility decreased. These (sub) microstructural alterations reduced corrosion resistance (lower breakdown potential and weaker passive layer) and increased crack susceptibility (higher surface crack density and more severe surface cracking).
- Surface cracking was preferentially initiated at the interface between subgranular cells' matrix and the cells' borders, possibly due to the presence of relatively higher density of defects in these regions such as dislocation densities, nano carbides and nanovoids.
- The corrosion morphology of the as-built specimens exhibited selective dissolution of the subgrain matrix regardless of laser power settings. However, a slightly more severe corrosion attack was observed for samples fabricated using 125 W. Additionally, a higher degree of selective dissolution was observed around laser track boundaries due to the accumulation of point defects and higher dislocation densities in those regions.

Overall, this study focused on the critical role played by microstructural alterations caused by slight variations in laser power in influencing the corrosion behaviour and crack initiation susceptibility of L-PBF-processed Ni-Fe-Cr alloy 718.

CRediT authorship contribution statement

Arshad Yazdanpanah: Conceptualization, Data curation, Formal analysis, Investigation, Methodology, Software, Validation, Visualization, Writing – original draft, Writing – review & editing. **Reynier I. Revilla:** Conceptualization, Data curation, Formal analysis, Investigation, Writing – review & editing, Writing – original draft. **Mattia Franceschi:** Investigation. **Alberto Fabrizi:** Investigation. **Saeed Khademzadeh:** Resources. **Mona Khodabakhshi:** Data curation, Formal analysis, Investigation, Software, Visualization. **Iris De Graeve:** Conceptualization, Funding acquisition, Supervision. **Manuele Dabalà:** Conceptualization, Funding acquisition, Project administration, Supervision, Writing – review & editing.

Declaration of Competing Interest

The authors declare that they have no known competing financial interests or personal relationships that could have appeared to influence the work reported in this paper.

Data availability

The raw data required to reproduce these findings can be made available upon reasonable request.

Acknowledgement

This work was supported by the University of Padova, Department of Industrial Engineering, and Department of Materials and Chemistry, Research Group Electrochemical and Surface Engineering, Vrije Universiteit Brussel (VUB). Mattia Venturin from the University of Padova is also acknowledged for his contribution to sample preparation.

References

[1] S. Novak, M. Podest, Nuclear power plant ageing and life extension: safety aspects, IAEA Bull. 29 (1987) 31–33.
[2] M. Brandt (Ed.), Laser Additive ManufacturingMaterials, Design, Technologies, and Applications, 1st Edition, 2016, pp. 2–7.
[3] P. Tao, H. Li, B. Huang, Q. Hu, S. Gong, Q. Xu, The crystal growth, intercellular spacing and microsegregation of selective laser melted Inconel 718 superalloy, Vacuum 159 (2019) 382–390, https://doi.org/10.1016/j.vacuum.2018.10.074.
[4] S. Holland, X. Wang, J. Chen, W. Cai, F. Yan, L. Li, Multiscale characterization of microstructures and mechanical properties of Inconel 718 fabricated by selective laser melting, J. Alloys Compd. 784 (2019) 182–194.
[5] D. Gu, Q. Shi, K. Lin, L. Xi, Microstructure and performance evolution and underlying thermal mechanisms of Ni-based parts fabricated by selective laser melting, Addit. Manuf. 22 (2018) 265–278, https://doi.org/10.1016/j.addma.2018.05.019.
[6] R. Vincent, Precipitation around welds in the nickel-base superalloy, Inconel 718, Acta Metall. 33 (1985) 1205–1216, https://doi.org/10.1016/0001-6160(85)90231-7.
[7] W.M. Tucho, P. Cuvillier, A. Sjolyst-Kverneland, V. Hansen, Microstructure and hardness studies of Inconel 718 manufactured by selective laser melting before and after solution heat treatment, Mater. Sci. Eng. A 689 (2017) 220–232, https://doi.org/10.1016/j.msea.2017.02.062.
[8] E. Chlebus, K. Gruber, B. Kuźnicka, J. Kurzac, T. Kurzynowski, Effect of heat treatment on the microstructure and mechanical properties of Inconel 718 processed by selective laser melting, Mater. Sci. Eng. A 639 (2015) 647–655, https://doi.org/10.1016/j.msea.2015.05.035.
[9] L.Y. Wang, Z.J. Zhou, C.P. Li, G.F. Chen, G.P. Zhang, Comparative investigation of small punch creep resistance of Inconel 718 fabricated by selective laser melting, Mater. Sci. Eng. A 745 (2019) 31–38.
[10] V.S. Raja, T. Shoji, Stress Corrosion Cracking: Theory and Practice, Elsevier, 2011.
[11] S. Lozano-Perez, P. Rodrigo, L.C. Gontard, Three-dimensional characterization of stress corrosion cracks, J. Nucl. Mater. 408 (2011) 289–295.
[12] H. Coriou, L. Grall, C. MAHlEU, M. Pelas, Sensitivity to stress corrosion and intergranular attack of high-nickel austenitic alloys, Corrosion 22 (1966) 280–290.
[13] X. Lou, M. Song, P.W. Emigh, M.A. Othon, P.L. Andresen, On the stress corrosion crack growth behaviour in high temperature water of 316 L stainless steel made by laser powder bed fusion additive manufacturing, Corros. Sci. 128 (2017) 140–153, https://doi.org/10.1016/j.corsci.2017.09.017.
[14] X. Lou, P.L. Andresen, R.B. Rebak, Oxide inclusions in laser additive manufactured stainless steel and their effects on impact toughness and stress corrosion cracking behavior, J. Nucl. Mater. 499 (2018) 182–190, https://doi.org/10.1016/j.jnucmat.2017.11.036.
[15] M. Song, M. Wang, X. Lou, R.B. Rebak, G.S. Was, Radiation damage and irradiation-assisted stress corrosion cracking of additively manufactured 316 L

stainless steels, J. Nucl. Mater. 513 (2019) 33–44, https://doi.org/10.1016/j.jnucmat.2018.10.044.
[16] M. McMurtrey, C. Sun, R.E. Rupp, C.-H. Shiau, R. Hanbury, N. Jerred, R. O'Brien, Investigation of the irradiation effects in additively manufactured 316 L steel resulting in decreased irradiation assisted stress corrosion cracking susceptibility, J. Nucl. Mater. 545 (2021), 152739, https://doi.org/10.1016/j.jnucmat.2020.152739.
[17] E.K. Karasz, J. Taylor, D.M. Autenrieth, P. Reu, K. Johnson, M. Melia, P. Noell, Measuring the residual stress and stress corrosion cracking susceptibility of additively manufactured 316 L by ASTM G36-94, Corrosion 78 (2021) 3–12, https://doi.org/10.5006/3894.
[18] V. Cruz, Y. Qiu, N. Birbilis, S. Thomas, Stress corrosion cracking of 316 L manufactured by laser powder bed fusion in 6 % ferric chloride solution, Corros. Sci. 207 (2022), 110535, https://doi.org/10.1016/j.corsci.2022.110535.
[19] M. Cabrini, S. Lorenzi, C. Testa, F. Carugo, T. Pastore, D. Manfredi, S. Biamino, G. Marchese, S. Parizia, F. Scenini, Stress corrosion cracking of additively manufactured Alloy 625, Materials (Basel) 14 (2021) 6115, https://doi.org/10.3390/ma14206115.
[20] R.W. Staehle, in: Stress Corrosion Cracking of Nickel Based Alloys in Water-Cooled Nuclear Reactors, Elsevier, 2016, pp. 3–131.
[21] J. Yang, M. Song, L.R. Hawkins, X. Liu, L. He, X. Lou, Effects of heat treatment on corrosion fatigue and stress corrosion crack growth of additive-manufactured Alloy 800H in high-temperature water, Corros. Sci. 191 (2021), 109739, https://doi.org/10.1016/j.corsci.2021.109739.
[22] X. Zhong, S.C. Bali, T. Shoji, Accelerated test for evaluation of intergranular stress corrosion cracking initiation characteristics of non-sensitized 316 austenitic stainless steel in simulated pressure water reactor environment, Corros. Sci. 115 (2017) 106–117, https://doi.org/10.1016/j.corsci.2016.11.019.
[23] D. Song, S.W. Kim, S.S. Hwang, D.J. Kim, C.H. Lee, In situ investigation of intergranular stress corrosion cracking initiation and coalescence and effects of geometric and microstructural characteristics, Corrosion 74 (2018) 1385–1394, https://doi.org/10.5006/2872.
[24] K. Arioka, Role of cavity formation on long-term stress corrosion cracking initiation: a review, Corrosion 76 (2020) 142–175.
[25] J.P. Park, S.C. Yoo, J.H. Kim, C.B. Bahn, Development of probabilistic primary water stress corrosion cracking initiation model for alloy 182 welds considering thermal aging and cold work effects, Nucl. Eng. Technol. 53 (2021) 1909–1923, https://doi.org/10.1016/j.net.2020.12.005.
[26] S.S. Hwang, M.J. Choi, S.W. Kim, D.J. Kim, Review of factors affecting IASCC initiation of stainless steel in PWRs, Corros. Sci. Technol. 20 (2021) 210–229, https://doi.org/10.14773/cst.2021.20.4.210.
[27] Z. Que, T. Saario, A. Toivonen, U. Ehrnstén, Stress corrosion cracking initiation susceptibility of Alloy 182 with different surface treatments, Corros. Sci. 196 (2022), 110037, https://doi.org/10.1016/j.corsci.2021.110037.
[28] G.B. Mazzei, M.G. Burke, D.A. Horner, F. Scenini, Lead-induced stress corrosion cracking (PbSCC) initiation in Alloy 690TT in caustic environment, Corros. Sci. 206 (2022), 110475, https://doi.org/10.1016/j.corsci.2022.110475.
[29] W. Kuang, S. Wang, X. Feng, H. Yue, Strain rate dependence of the effect of intergranular carbides on the resistance to stress corrosion cracking initiation of Alloy 690 in simulated PWR primary water, Corros. Sci. 206 (2022), https://doi.org/10.1016/j.corsci.2022.110502.
[30] I.E. Locci, H.K. Kwon, R.F. Hehemann, A.R. Troiano, Stress corrosion cracking initiation in ferritic stainless steels in a chloride environment, Corrosion 43 (1987) 465–470, https://doi.org/10.5006/1.3583886.
[31] G. Bombara, The role of oxide films in stress corrosion cracking initiation, Corros. Sci. 19 (1979) 991–999, https://doi.org/10.1016/S0010-938X(79)80089-X.
[32] A. Yazdanpanah, M. Franceschi, P. Rebesan, M. Dabalà, Correlation of lack of fusion pores with stress corrosion cracking susceptibility of L-PBF 316L: effect of surface residual stresses, Materials (Basel) 15 (2022) 7151, https://doi.org/10.3390/ma15207151.
[33] A. Yazdanpanah, M. Franceschi, G. Bergamo, M. Bonesso, M. Dabalà, On the exceptional stress corrosion cracking susceptibility of selective laser melted 316 L stainless steel under the individual effect of surface residual stresses, Eng. Fail. Anal. 136 (2022), 106192, https://doi.org/10.1016/j.engfailanal.2022.106192.
[34] A. Yazdanpanah, M. Lago, C. Gennari, M. Dabalà, Stress corrosion cracking probability of selective laser melted 316 L austenitic stainless steel under the effect of grinding induced residual stresses, Metals (Basel) 11 (2021) 327, https://doi.org/10.3390/met11020327.
[35] A. Yazdanpanah, M. Franceschi, R.I. Revilla, S. Khademzadeh, I. De Graeve, M. Dabalà, Revealing the stress corrosion cracking initiation mechanism of Alloy 718 prepared by laser powder bed fusion assessed by microcapillary method, Corros. Sci. 208 (2022), 110642, https://doi.org/10.1016/j.corsci.2022.110642.
[36] C.A. Schneider, W.S. Rasband, K.W. Eliceiri, NIH Image to ImageJ: 25 years of image analysis, Nat. Methods 9 (2012) 671–675.
[37] J.H.W. De Wit, Local potential measurements with the SKPFM on aluminium alloys, Electrochim. Acta 49 (2004) 2841–2850.
[38] R.I. Revilla, J. Liang, S. Godet, I.D. Graeve, Local corrosion behavior of additive manufactured AlSiMg alloy assessed by SEM and SKPFM, J. Electrochem. Soc. 164 (2016), https://doi.org/10.1149/2.0461702jes. C27.
[39] R.I. Revilla, Methods—On the application of ambient scanning kelvin probe force microscopy to understand micro-galvanic corrosion phenomena: interpretation and challenges, J. Electrochem. Soc. 170 (1) (2023), 011501, https://doi.org/10.1149/1945-7111/acafab.
[40] P.L. Andresen, Understanding and predicting stress corrosion cracking (SCC) in hot water, in: Stress Corrosion Cracking of Nickel Based Alloys in Water-Cooled Nuclear Reactors, Elsevier, 2016, pp. 169–238.
[41] A. Yazdanpanah, L. Pezzato, M. Dabalà, Stress corrosion cracking of AISI 304 under chromium variation within the standard limits: failure analysis implementing microcapillary method, Eng. Fail. Anal. 142 (2022), 106797, https://doi.org/10.1016/j.engfailanal.2022.106797.
[42] M. Klinger, A. Jäger, *Crystallographic Tool Box* (*CrysTBox*): automated tools for transmission electron microscopists and crystallographers, J. Appl. Crystallogr. 48 (2015) 2012–2018, https://doi.org/10.1107/S1600576715017252.
[43] R.I. Revilla, H. Terryn, I. De Graeve, On the use of SKPFM for in situ studies of the repassivation of the native oxide film on aluminium in air, Electrochem. Commun. 93 (2018) 162–165, https://doi.org/10.1016/j.elecom.2018.07.010.
[44] Y. Li, D. Gu, Parametric analysis of thermal behavior during selective laser melting additive manufacturing of aluminum alloy powder, Mater. Des. 63 (2014) 856–867.
[45] R. Li, Y. Shi, J. Liu, H. Yao, W. Zhang, Effects of processing parameters on the temperature field of selective laser melting metal powder, Powder Metall. Metal Ceram. 48 (2009) 186–195.
[46] P. Yuan, D. Gu, Molten pool behaviour and its physical mechanism during selective laser melting of TiC/AlSi10Mg nanocomposites: simulation and experiments, J. Phys. D Appl. Phys. 48 (2015), 035303.
[47] I. Yadroitsev, A. Gusarov, I. Yadroitsava, I. Smurov, Single track formation in selective laser melting of metal powders, J. Mater. Process. Technol. 210 (2010) 1624–1631.
[48] D.D. Gu, W. Meiners, K. Wissenbach, R. Poprawe, Laser additive manufacturing of metallic components: materials, processes and mechanisms, Int. Mater. Rev. 57 (2012) 133–164.
[49] O. Gokcekaya, T. Ishimoto, S. Hibino, J. Yasutomi, T. Narushima, T. Nakano, Unique crystallographic texture formation in Inconel 718 by laser powder bed fusion and its effect on mechanical anisotropy, Acta Mater. 212 (2021), 116876, https://doi.org/10.1016/j.actamat.2021.116876.
[50] H.H. Zhu, L. Lu, J.Y.H. Fuh, Study on shrinkage behaviour of direct laser sintering metallic powder, Proc. Inst. Mech. Eng. Part B J. Eng. Manuf. 220 (2006) 183–190.
[51] R.I. Revilla, M. Van Calster, M. Raes, G. Arroud, F. Andreatta, L. Pyl, P. Guillaume, I. De Graeve, Microstructure and corrosion behavior of 316 L stainless steel prepared using different additive manufacturing methods: a comparative study bringing insights into the impact of microstructure on their passivity, Corros. Sci. 176 (2020), 108914, https://doi.org/10.1016/j.corsci.2020.108914.
[52] L. Liu, Q. Ding, Y. Zhong, J. Zou, J. Wu, Y.-L. Chiu, J. Li, Z. Zhang, Q. Yu, Z. Shen, Dislocation network in additive manufactured steel breaks strength–ductility trade-off, Mater. Today 21 (2018) 354–361, https://doi.org/10.1016/j.mattod.2017.11.004.
[53] S. Lozano-Perez, D.W. Saxey, T. Yamada, T. Terachi, Atom-probe tomography characterization of the oxidation of stainless steel, Scr. Mater. 62 (2010) 855–858, https://doi.org/10.1016/j.scriptamat.2010.02.021.
[54] Z. Shen, E. Roberts, N. Saravanan, P. Karamched, T. Terachi, T. Yamada, S. Wu, E. Tarleton, D.E. Armstrong, P.J. Withers, On the role of intergranular nanocavities in long-term stress corrosion cracking of Alloy 690, Acta Mater. 222 (2022), 117453.
[55] C.T. Sims, N.S. Stoloff, W.C. Hagel, Superalloys II, Wiley, 1987.
[56] O. Gokcekaya, N. Hayashi, T. Ishimoto, K. Ueda, T. Narushima, T. Nakano, Crystallographic orientation control of pure chromium via laser powder bed fusion and improved high temperature oxidation resistance, Addit. Manuf. 36 (2020), 101624, https://doi.org/10.1016/j.addma.2020.101624.
[57] R. Bender, D. Féron, D. Mills, S. Ritter, R. Bäßler, D. Bettge, I. De Graeve, A. Dugstad, S. Grassini, T. Hack, Corrosion challenges towards a sustainable society, Mater. Corros. 73 (2022) 1730–1751.